## **Ambient Infrasound Noise, Station** Performance, and Their Relation to Land **Cover across Alaska**

Kenneth A. Macpherson\*1<sup>©</sup>, Juliann R. Coffey<sup>1</sup>, Alex J. Witsil<sup>1</sup>, David Fee<sup>1</sup>, Stephen Holtkamp<sup>2</sup>, Scott Dalton<sup>2</sup>, Heather McFarlin<sup>2</sup>, and Michael West<sup>2</sup>

#### **Abstract**

The addition of 108 infrasound sensors—a legacy of the temporary USArray Transportable Array (TA) deployment—to the Alaska regional network provides an unprecedented opportunity to quantify the effects of a diverse set of site conditions on ambient infrasound noise levels. TA station locations were not chosen to optimize infrasound performance, and consequently span a dramatic range of land cover types, from temperate rain forest to exposed tundra. In this study, we compute power spectral densities for 2020 data and compile new ambient infrasound low- and high-noise models for the region. In addition, we compare time series of root-mean-squared (rms) amplitudes with wind data and high-resolution land cover data to derive noise-wind speed relationships for several land cover categories. We observe that noise levels for the network are dominated by wind, and that network noise is generally higher in the winter months when storms are more frequent and the microbarom is more pronounced. Wind direction also exerts control on noise levels, likely as a result of infrasound ports being systematically located on the east side of the station huts. We find that rms amplitudes correlate with site land cover type, and that knowledge of both land cover type and wind speed can help predict infrasound noise levels. Our results show that land cover data can be used to inform infrasound station site selection, and that wind-noise models that incorporate station land cover type are useful tools for understanding general station noise performance.

Cite this article as Macpherson, K. A., J. R. Coffey, A. J. Witsil, D. Fee, S. Holtkamp, S. Dalton, H. McFarlin, and M. West (2022). Ambient Infrasound Noise, Station Performance, and Their Relation to Land Cover across Alaska Seismol. Res. Lett. 93, 2239-2258, doi: 10.1785/0220210365.

**Supplemental Material** 

#### Introduction

Infrasound stations are typically located in sheltered areas to minimize wind-generated noise. For example, many of the International Monitoring System (IMS)'s infrasound array locations are carefully selected to use topographic features, such as mountains and dense forests to minimize the effects of wind and enhance their ability to detect faint signals generated by distant low-yield explosions (Christie et al., 2001). Siting stations in low-wind environments has long been recognized as an effective way to reduce noise in other monitoring regimes as well, such as in volcano infrasound (Fee and Matoza, 2013). In situations in which stations must be installed in exposed areas, such as when conforming to a geographic grid as with the IMS, the use of wind-noise reduction systems (WNRS) is critical for controlling ambient wind noise (Christie and Campus, 2009). These WNRS are spatial filters, usually composed of a system of pipes with multiple ports that incoherently average high-frequency noise (Walker and Hedlin, 2010). Because most infrasound deployments use careful site placement or WNRS to attenuate noise, there has been little opportunity to investigate the effects of suboptimal local site conditions and a lack of WNRS on infrasound

ambient noise. However, as of late 2020, over 100 infrasound stations—a legacy of the USArray Transportable Array (TA) -have been incorporated into the Alaska regional network (AK) (Alaska Earthquake Center, University of Alaska Fairbanks, 1987; IRIS Transportable Array, 2003). A regional infrasound network that is relatively dense and has a spatial extent on the order of thousands of kilometers is rare, although they are becoming more popular as a result of the relatively low costs associated with equipping existing seismic stations with single infrasound sensors. The establishment of this new regional infrasound network provides an opportunity to examine the infrasonic noise environment of a region with diverse geography and extreme weather conditions.

<sup>1.</sup> Wilson Alaska Technical Center, Geophysical Institute, University of Alaska Fairbanks, Fairbanks, Alaska, U.S.A., https://orcid.org/0000-0002-5521-6912 0002-0936-9977 (DF); 2. Alaska Earthquake Center, Geophysical Institute, University of Alaska Fairbanks, Fairbanks, Alaska, U.S.A., https://orcid.org/0000-0002-3829-

<sup>\*</sup>Corresponding author: kamacpherson@alaska.edu

<sup>©</sup> Seismological Society of America

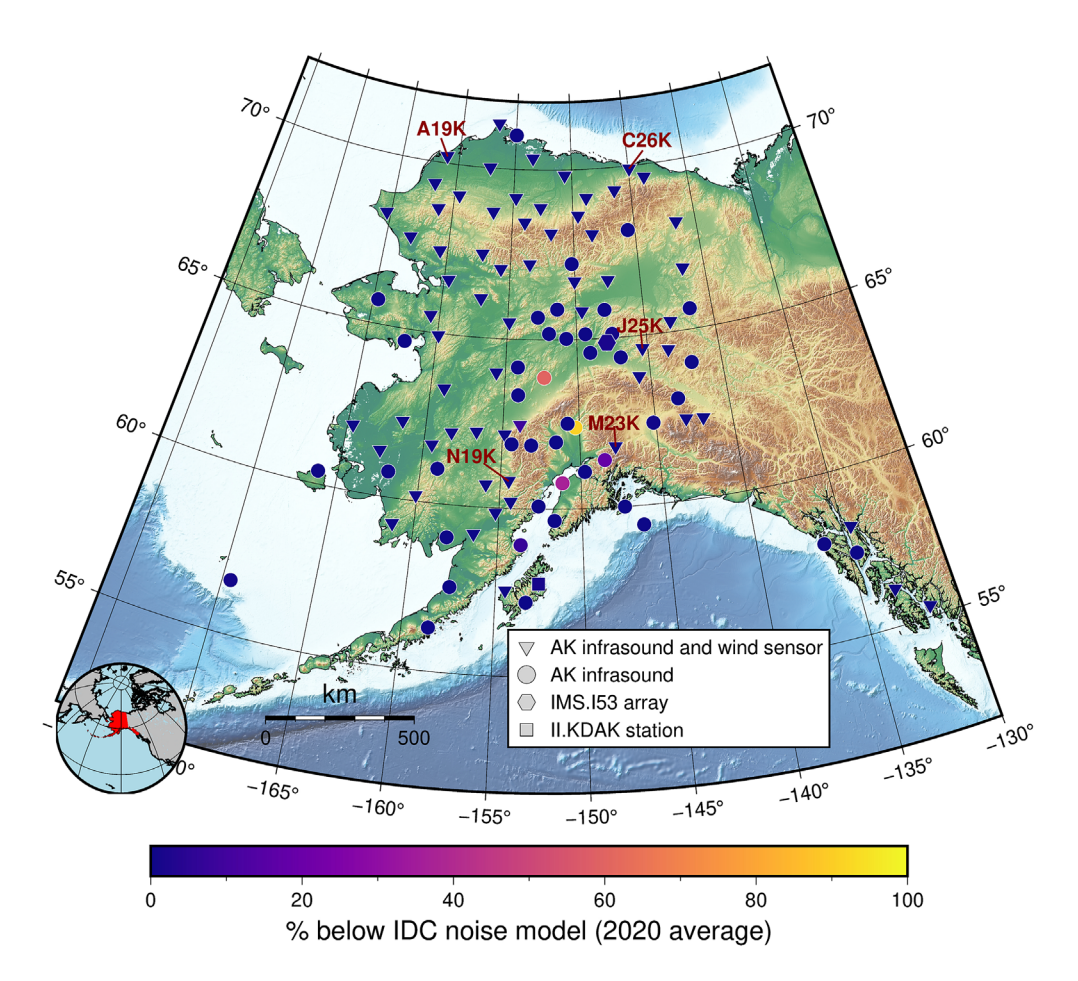


**Figure 1.** Map of Alaska showing all AK network stations equipped with infrasound sensors. Inset map at the lower left shows Alaska highlighted in red. Stations with colocated weather stations are marked with inverted triangles, whereas infrasound only sites are shown as circles. Also plotted are the Interantional Monitoring System array I53 (hexagon) and the Global Seismographic Network station KDAK (square). All symbols are colored by the average percentage of spectra below the International Data Center (IDC) noise model (Brown et al., 2012) for 2020. Although most stations have a very low percentage of spectra below the model, four stations exhibit a high percentage of low-amplitude spectra. Stations mentioned explicitly in the Data Quality section, Results of Modeling Noise as a Function of Wind Speed and Land Cover section, and Figure 8 are labeled. The color version of this figure is available only in the electronic edition.

The TA was a temporary deployment of 400 stations equipped with three-component broadband seismometers and a number of ancillary sensors, with approximately 50 km spacing and an aperture of 1000 km. The TA moved from west to east across the contiguous United States before a final deployment to Alaska (Melter et al., 1999; Busby and Aderhold, 2020). The Alaska TA deployment comprised 285 stations spaced roughly every 85 km with subsets of stations operating between 2014 and 2021 (Busby and Aderhold, 2020). In addition to a three-component broadband seismometer, each Alaska station was equipped with a Hyperion IFS-4132 infrasound sensor recording in real time at 20 samples per second (sps) and flat from the 10.0 Hz Nyquist frequency down to 0.02 Hz (Merchant, 2015). In addition, there was a 40.0 sps infrasound channel that was not telemetered in real time, but these data do

not appear to be available at the time of this writing. The infrasound sensor resided in the station hut and was connected to a single polyvinyl chloride diffuser port installed on the east side of the hut. Notably, the TA infrasound configuration did not include a WNRS. In addition, 143 of the sites were equipped Vaisala with WXT-520 WXT-536 weather sensor. These weather sensors recorded wind speed and direction, humidity, temperature, pressure, and rain and hail intensity. For a detailed schematic of a typical Alaska TA station, we refer the reader to Busby and Aderhold (2020). We also include a detailed image of a diffuser port in the Appendix (see Fig. A1).

Although the final TA station in Alaska ceased operation in May 2021, in early 2019 the Alaska Earthquake Center at the University of Alaska Fairbanks began adopting TA sites into the permanent regional AK network. By the end of 2020, a total of 108 infrasound-equipped sites had either been adopted into the AK network or upgraded during the TA project (Alaska Earthquake Center, University of Alaska Fairbanks, 1987). These stations

all retained their Hyperion infrasound sensor, but real-time sampling rates were increased to 40.0 sps. Of these, 70 are equipped with Vaisala weather stations. A network map showing the spatial distribution of this new regional infrasound network, which spans  $16^{\circ}$  of latitude from  $55.3^{\circ}$  to  $71.3^{\circ}$  and almost  $40^{\circ}$  of longitude from  $-169.6^{\circ}$  to  $-131^{\circ}$ , is shown in Figure 1.

In this study, we leverage data from the AK network to evaluate the infrasound noise levels of sites in the Alaska region (see Data and Resources). Because of the quasi-grid nature of the TA deployment and original seismological focus, sites were not chosen to optimize infrasound performance. Therefore, we are able to investigate the effects of a broad range of site conditions on noise levels. The absence of WNRS allows us to evaluate the viability of such a simple configuration in terms of ambient noise performance and

provides direct, unfiltered, observations of the infrasonic environment. Because of the low population density of Alaska, sites are relatively free of cultural noise, and the majority of such noise will be at frequencies above 8.0 Hz (Bird et al., 2021). Furthermore, the presence of colocated meteorological sensors at over half of the networks sites also presents an opportunity to evaluate the effects of wind on noise conditions and explore relationships between site placement, wind, and ambient noise. This characterization of ambient noise at such a diverse set of site conditions enhances our general understanding of expected station performance in less optimal locations.

#### **Methods**

Our primary tool for investigating the noise characteristics of the network is power spectral densities (PSDs) organized into probability density functions (PDFs). We compute PSD PDFs for station quality control (QC), for compilation of a regional ambient model, and for the calculation of time series of amplitudes in several frequency bands. We compute PSD estimates for all the 108 stations from hour-long segments of data sampled every 4 hr between 1 January 2020 and 1 January 2021. Using an entire year of data includes seasonal effects on noise characterization, whereas the 4 hr sampling rate resolves any diurnal effects (de Groot-Hedlin et al., 2010). We compute spectra using a method similar to McNamara and Buland (2004), as implemented in the ObsPy Python package, with the exception that we do not employ an additional differentiation step at the response removal stage that is conventional for converting seismic velocity data to acceleration (Beyreuther et al., 2010; Krischer et al., 2015). After conversion to decibels (dB), our PSDs have units of Pascals squared per Hertz (Pa<sup>2</sup>/Hz dB). To compute a single PSD for every hour considered, we used the default ObsPy parameter of 3600 s segment length. Hours with outages or gaps were left out of our PSD calculation. This strategy results in a dataset of over 210,000 PSDs.

#### **Data quality**

We use the PDFs for individual stations to conduct a data QC check. Stations that have a significant percentage of their spectra below a relevant ambient noise model are likely to have either inaccurate response information or some physical issue with the sensor (Casey et al., 2018). We compare PDFs to the global ambient acoustic model compiled by Brown et al. (2012) from IMS stations for the International Data Center (IDC). Because those stations employ WNRS and are often sited in low infrasonic noise areas, this is a conservative test for AK stations. The average percentage of spectra below the IDC noise model for 2020 is shown in Figure 1. This analysis identified clear problems with four stations, which exhibited notable percentages of their spectra below the IDC low-noise model for the year (see Fig. A2 for spectra of these stations).

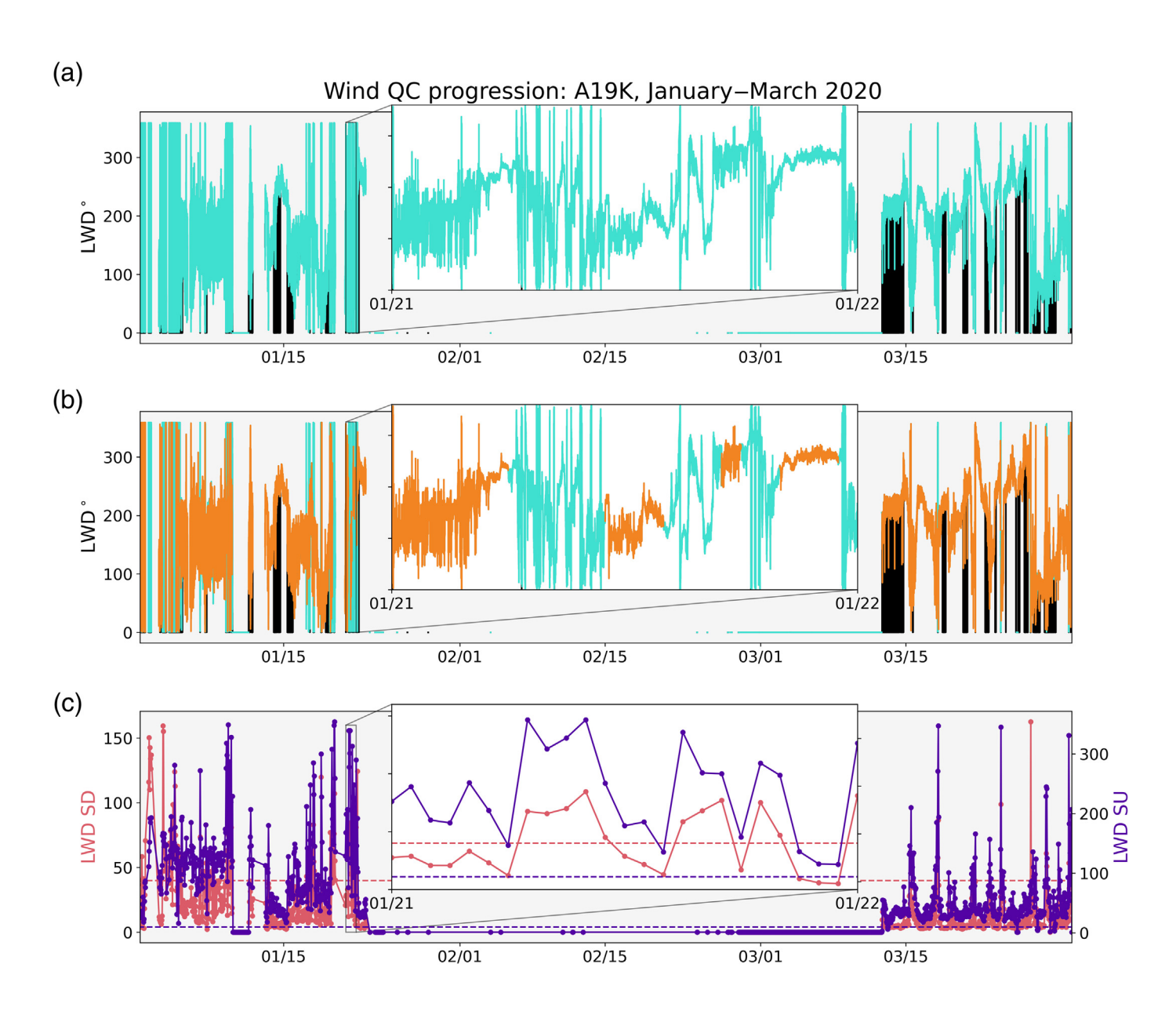
We suspect that there are incorrect responses in the metadata for these stations. Therefore, these four stations are removed from further analysis.

Data QC checks are also applied to hour-long segments of wind speed (channel code LWS) and direction (channel code LWD) waveforms to remove absent or unrealistic data from analysis. Values that are either too large or too small to represent physical quantities, identically zero, or fluctuate drastically from high to low values within a short time duration are indicators of nonphysical data. Our wind data QC workflow identifies and removes these characteristics. Several steps in these methods require thresholds, or other arbitrary time windows of analysis, which were established through trial and error. Given these methods are new, we expect a more rigorous investigation into optimizing these values in future work.

The first step of our wind QC workflow uses the common seismic QC metric sample unique (SU), which is simply the number of unique values in a data segment (Casey et al., 2018). Although the metric is designed for higher sample rates, we found, even for 1.0 sps weather data, a very low SU value is a reliable indicator of a malfunctioning sensor. Hour-long sengments of data are removed from analysis, if SU is less than ten samples for LWD data or equal to one point for LWS data—values that were determined by trial and error. We also discard weather data segments with non-physical amplitudes. If LWS data are less than zero or greater than 100 m/s, or if LWD data are less than zero or greater than 360°, those points are characterized as nonphysical and are discarded.

Often, the wind data fluctuate from high to low values rapidly because of many repeating and physically unrealistic zero points. We, therefore, replace data points that are equal to zero with the average of the surrounding two data points. Removing these zero points usually results in data that do not fluctuate so rapidly and are, therefore, better suited for averaging in later analysis. However, some of the data still contain large fluctuations even after zeros are removed, as shown in Figure 2a. In this example at station A19K, replacing the zeros removes the large fluctuations from the waveform in March 2020, but there are still large swings in January.

To address these data fluctuations, we calculate the standard deviation (SD) on the zeros removed data to discard hours that contain high SD values for either the LWS or LWD data. An hour-long segment of data is kept if SD is less than 40.0 for LWD data and less than 4.0 for LWS data. Like the thresholds for SU, the SD thresholds were chosen experimentally, based on their effectiveness at removing periods with large data swings. Figure 2b shows a comparison between the raw data, data with nonphysical values and zeros removed, and the data retained after additionally removing hours of high SD, in which data with large swings are not kept. This final step in the QC process is important in removing time periods of high



fluctuations, like those on 21 January. Figure 2c shows the calculated SU and SD values throughout the month, and how thresholding allows us to eliminate highly fluctuating data and empty data time periods. This QC process results in a physically reasonable, high-quality wind dataset that is utilized for noise modeling described in the following.

#### Constructing ambient infrasound noise models

Noise models are useful for estimating station performance and as inputs to network detection thresholds (Green and Bowers, 2010; Le Pichon *et al.*, 2012). Station operators can quickly evaluate noise performance by comparing spectra to the noise models to determine if a station is particularly noisy, identify potential system response issues, or determine if amplitudes are within the expected limits. Several studies have used recordings from the globally distributed IMS stations to construct global ambient infrasound noise models. Bowman *et al.* (2005) constructed low-, high-, and median-

**Figure 2.** Wind data quality control (QC) for station A19K from January to March 2020. (a) Raw (black) and retained (turquoise) waveforms after removing hourly time periods containing nonphysically high or low values, and removing all zeros in the data. (b) Final retained waveform (orange) after all stages of QC, including removing hours of high standard deviation (SD) from zero-removed data, along with data from panel (a). (c) Pink circles show the average SD, and purple circles show the average sample unique (SU) for the given hour. Dashed red and blue lines show the high SD and low SU thresholds, 40 and 1, respectively. Insets on each panel show a day-long period in January in which the full QC process was necessary for eliminating noisy time periods of wind data. The color version of this figure is available only in the electronic edition.

noise models from one year of data from 2003 recorded at 10 WNRS-equipped stations. Their models were constructed from PSDs computed between 0.03 and 7.0 Hz, and they observed large seasonal variations in the noise spectra. A

similar analysis by Brown *et al.* (2012) used hour-long sections of data from 21 IMS stations sampled evenly across days during 2010. The low- and high-noise curves from the Brown model generally agree with the Bowman model. Recent models compiled by Marty *et al.* (2021) used data from a subset of the IMS network, and are unique in that they include very low frequencies (down to  $10^{-5}$  Hz) and remove the response imposed by the WNRS.

We employed a method similar to Brown *et al.* (2012) to construct ambient noise models for the Alaska region using 2020 data from the 104 properly functioning stations. We only use data from time periods when stations were part of the AK network for construction of the models to leverage the higher sample rate of 40.0 sps. We combined all PSDs computed from each station into a single PDF, resulting in a total of 140,371 PSDs.

For 113 frequencies, evenly sampled in log space between 0.05 and 13.0 Hz, we found the 5th, 50th, and 95th percentiles of all contributing PSDs. The curve for the new low-noise model was extracted by finding the minimum of all the 5th-percentile values for each frequency bin. Similarly, the high-noise model curve is the maximum of all the 95th-percentile curves at each frequency bin, and the median is the median of all the 50th-percentile values in each frequency bin.

## Constructing time series of root-mean-squared (rms) amplitudes

To develop year-long noise time series and to investigate wind-noise relationships, we extract the rms amplitudes from the PDFs for specific frequency domains. Parseval's theorem equates the integral of the square of a function with the integral of the square of its transform, insuring that energy is constant between the time and frequency domains (Gubbins, 2004). Therefore, rms amplitude may be computed as

$$rms_{f_1,f_2} = \sqrt{\int_{f_1}^{f_2} |PSDdf|},$$
 (1)

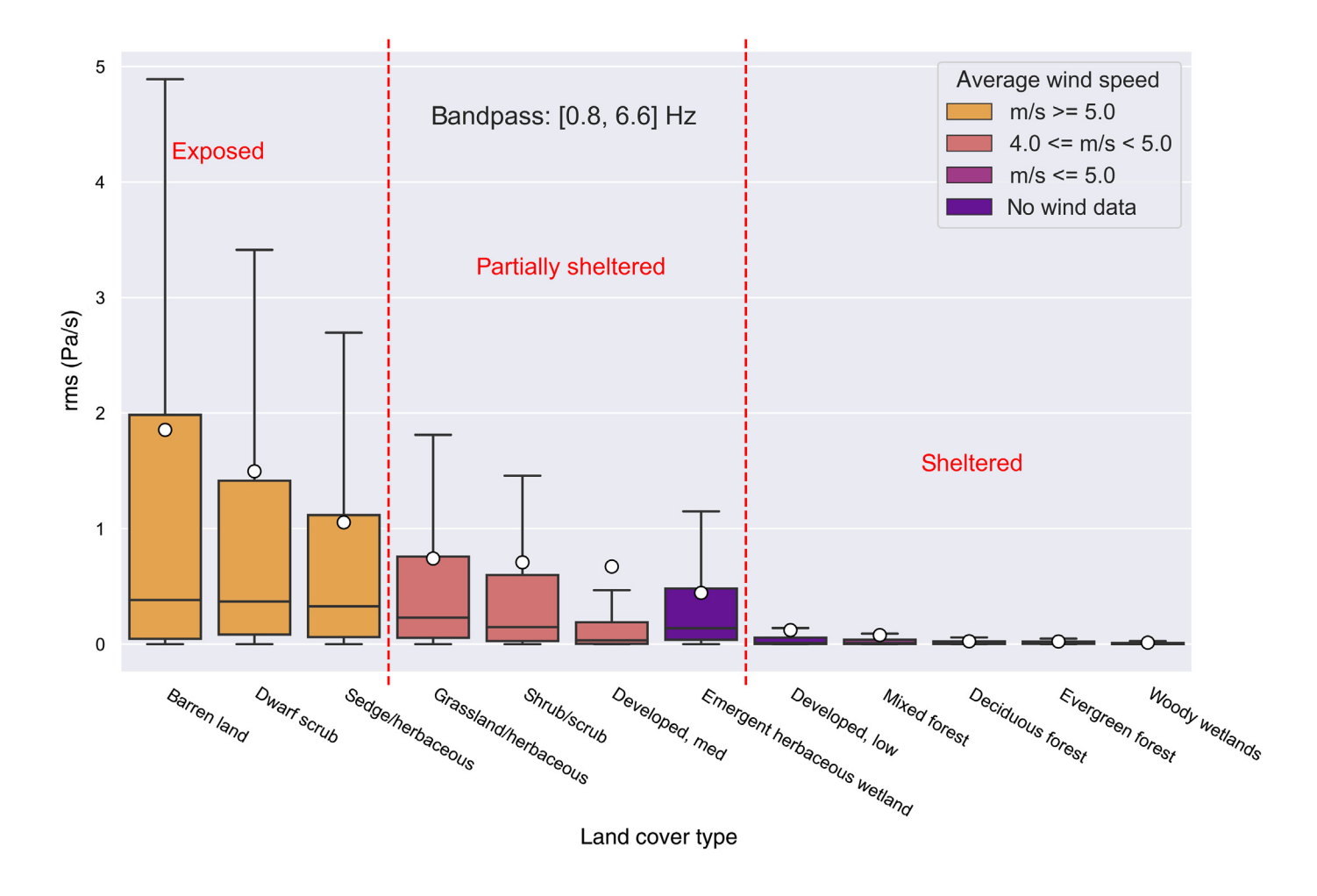
in which  $f_1$  and  $f_2$  are the high- and low-frequency bounds, respectively (Lecocq et al., 2020; Guenaga et al., 2021). Because we are examining discrete data, we approximate the definite integral in equation (1) using the SciPy implementation of the composite Simpsons' rule. This implementation is able to accommodate an odd number of segments using the average value of trapazoidal rules used on the first and last intervals (Virtanen et al., 2020). We calculate rms amplitudes for three separate passbands; the [0.01, 0.1] Hz band explores frequencies in which the WNRS of IMS stations are less effective, allowing us to compare noise with the I53 IMS array located in interior Alaska; the [0.1, 0.4] Hz passband examines noise in the microbarom band, whereas the [0.8, 6.6] Hz passband avoids the microbarom

peak of around 0.2 Hz and includes relatively high frequencies (Christie and Campus, 2009). The low-pass cutoff of 6.6 Hz is chosen due to the fact that many stations were still part of network TA for a portion of 2020, and so currently available data employed a 20.0 sps sampling rate. The McNamara and Buland (2004) method only considers frequencies below Nyquist×(2/3) = 10.0×(2/3) to avoid effects from digitizer finite impulse response filters, limiting our maximum frequency to 6.6 Hz in the current analysis.

We also examine the ability of stations in the network to observe the microbarom—a spectral peak around 0.2 Hz that is generated by waves at the ocean-atmosphere interface (Donn and Posmentier, 1967). We do this by fitting a line to the PSD curve in the microbarom band of 0.1-0.4 Hz. Linear fitting to spectra in the microseismic band is a standard data quality metric that is typically used to identify seismic sensors that are not recording ground motions (Casey et al., 2018). For infrasound sensors that are experiencing a noisy period due to elevated wind, the spectral segment will tend to be linear and will return a low residual after fitting the line. However, if a well-developed microbarom is present, the linear fit will be poor, and a large residual will be returned. By plotting these residuals with time, we are able to estimate time periods when the microbarom was likely present using a simple and understandable fitting algorithm.

## Developing relationships between noise, wind, and land cover type

We determine the prevalent land cover type at each AK infrasound station using the 2016 Alaska National Land Cover Database (Dewitz, 2019) and use it to investigate the effects of site conditions on rms amplitudes (see Data and Resources). This land cover dataset was compiled using change detection—a way to analyze the spectra of Landsat image pairs, between 2011 and 2015, and consists of 19 distinct land cover types that are available as raster data at 30 m resolution. We sampled this raster at all station locations to assign land cover types to each. The station locations span 12 distinct land cover types, representing very diverse conditions from dense, deciduous forest to exposed tundra. Comparing station land cover type with mean rms amplitudes for 2020 indicates that land cover has a dramatic effect on the noise characteristics of a station (see Fig. 3 for plot in the [0.8, 6.6] Hz passband, and Fig. A3 for additional passbands). More sheltered (forested) sites clearly experience reduced wind speeds and consequently lower noise levels. Inspection of Figure 3 also suggests that sites may be organized into three broad categories based on land cover type and noise characteristics. We designate these three categories as sheltered, partially sheltered, and exposed, and develop models for estimating rms as a function of wind speed for each land cover category and passband. Partitioning the dataset of hourly rms observations and hourly average wind speed



into the three categories, we obtained 110,355 observations for the exposed category, 66,282 for the partially sheltered category, and 11,907 for the sheltered category. We extracted the noise-wind models by organizing the average wind speed-rms pairs into 2D histograms similar to Le Pichon et al. (2009) and found the median values of the distribution (see Fig. 4). The shape of the medians in log space is complex, with several concavity changes apparent in most of the nine models. These medians are smoothed via a local polynomial filter. Finally, we employ a nonlinear regression on the smoothed median values to extract the coefficients for the best fitting seventh-degree polynomial that describes rms as a function of wind speed. The high-degree polynomial is necessary to capture the complexity of the empirical relationship. The nine noise-wind models from the three passbands and three land cover categories are shown by the solid green lines in Figure 4. The coefficients of the models are listed in Table 1.

#### Results

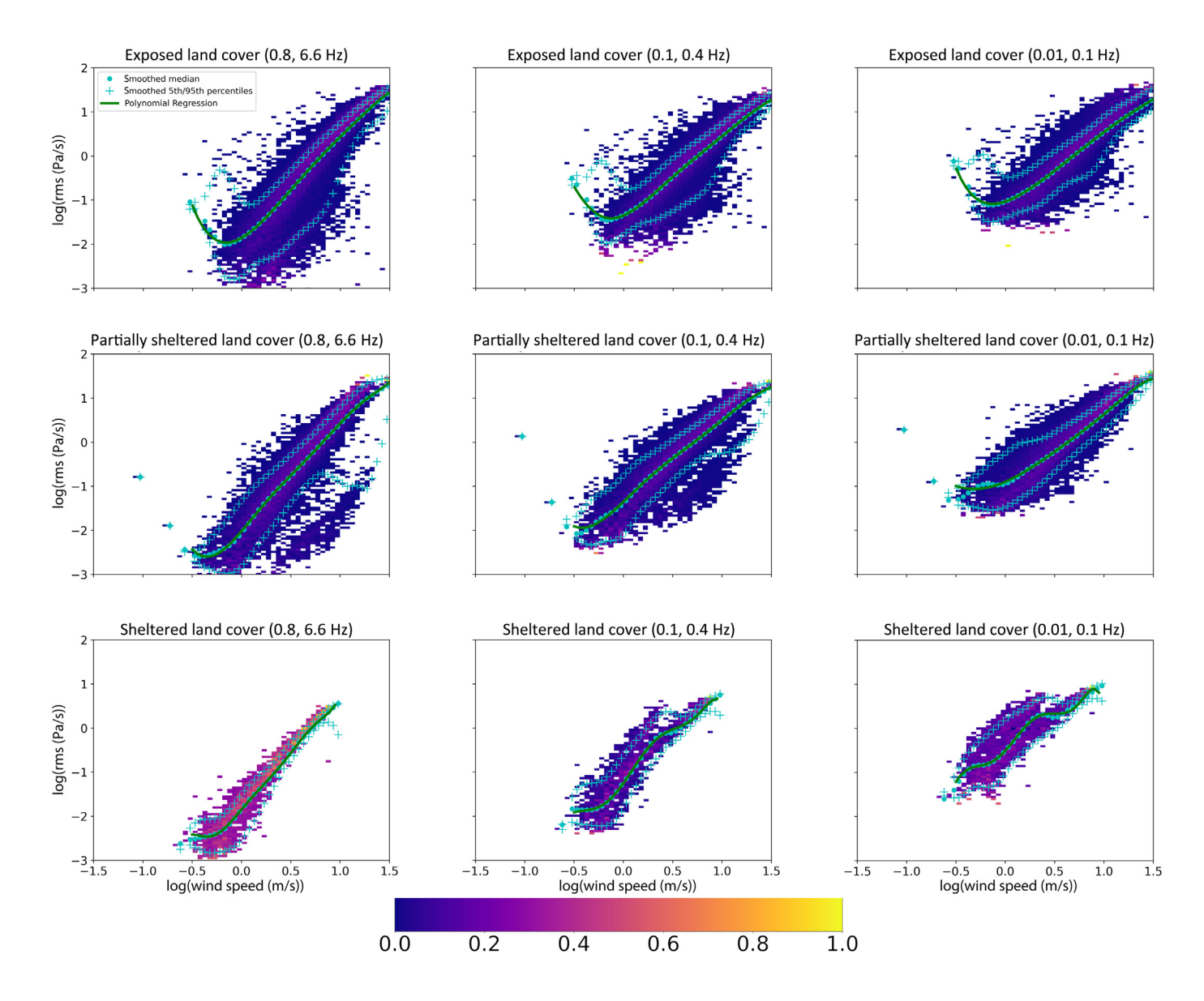
In this section, we describe the results from the AK infrasound network PSD PDFs analysis. We present an ambient infrasound model for the Alaska region, examine rms time series for each station, investigate likely microbarom presence

**Figure 3.** Root-mean-squared (rms) infrasound amplitude for 2020 binned by station land cover for the [0.8, 6.6] Hz passband. The upper and lower edges of the boxes denote the third and first quartiles, respectively. The horizontal line in each box denotes the medians, whereas the means are shown by white circles. The bars extend to 1.5 times the interquartile range. For clarity, outliers are not plotted. Boxes are colored by mean wind speed categories from the 2020 data. The color version of this figure is available only in the electronic edition.

in the spectra, and demonstrate the effectiveness of our models for estimating rms as a function of wind speed and land cover.

# An ambient infrasound model for the Alaska region

The models derived from the 2020 PSD PDFs are shown in Figure 5, along with the IDC model from Brown *et al.* (2012) for comparison. We term our model the "AK noise model." AK noise levels span a wide range: 50 dB at 0.05 Hz and 120 dB at 10.0 Hz, and show similar trends as the IDC noise models. The low-noise curve of the new ambient



model is comparable to the IDC low-noise model, particularly above about 0.1 Hz, although it does differ by up to 10 dB at lower frequencies. Our new model exhibits a prominent microbarom peak in the low-noise curve centered on 0.2 Hz, in agreement with the IDC model. As expected, given the lack of WNRS and spatial distribution across a wide range of environments, our high-noise model curve differs significantly from the IDC model. These differences are the most prevalent at higher frequencies, in which the AK noise model is as much as 30 dB higher. This high-frequency noise is likely imposed predominately by wind, and is subdued in the IDC model due to the use of IMS stations equipped with WNRS and sited in low-wind areas. The standard 18 m, 96-port rosette pipe array at IMS stations reduce uncorrelated wind noise by 20 dB (Alcoverro and Le Pichon, 2005). Therefore, the AK infrasound network likely has a higher noise environment than the IMS by ~10 db at both the high and low frequencies. There is closer agreement between the two high-noise models below around 0.1 Hz-frequencies in

**Figure 4.** Two-dimensional histograms showing relationships between observed wind speed and rms noise for 2020. The bins have been normalized to indicate the density of observations in each bin, with warmer colors indicating more observations. The top row is sites in the exposed land cover category, middle row is partially exposed, and bottom row is sheltered sites. The columns show the three passbands: [0.01, 0.1], [0.1, 0.4], and [0.8, 6.6] Hz. The smoothed median for each dataset is shown by cyan circles, the 5th and 95th percentiles are shown by cyan crosses, and a solid green line denotes the noise—wind model derived by a nonlinear regression of the smoothed median. The color version of this figure is available only in the electronic edition.

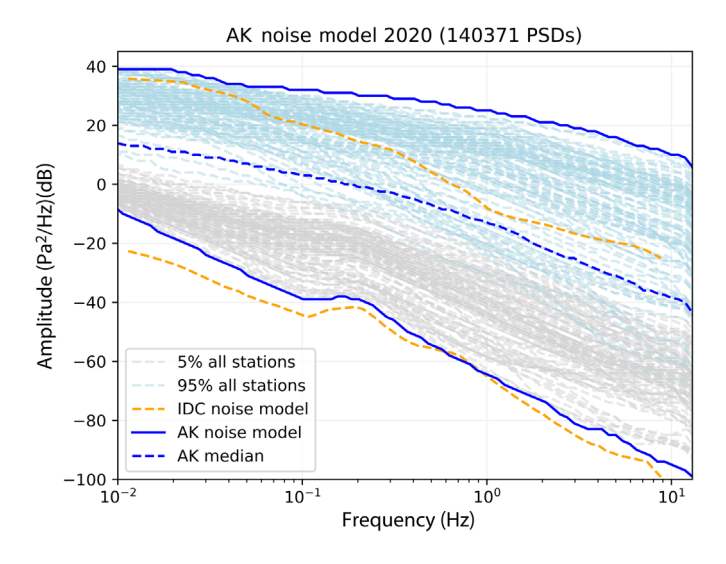
which the IMS WNRS are less effective. Our new mediannoise curve has a general roll-off of 1/f and lies below but relatively close to the IDC high-noise model. The new ambient infrasound models are available as a supplemental material to this article.

TABLE 1

Coefficients for the Nine Noise–Wind Models Described in the Developing Relationships between Noise, Wind, and Land Cover Type section

<b>Land Cover</b>									
Category	Passband	c <sub>1</sub>	c <sub>2</sub>	c <sub>3</sub>	<b>c</b> <sub>4</sub>	<b>c</b> <sub>5</sub>	<b>c</b> <sub>6</sub>	<b>c</b> <sub>7</sub>	<b>c</b> <sub>8</sub>
Exposed	0.01, 0.1	-0.049790	0.512101	-1.638147	2.622633	-2.853072	2.212958	0.772919	-1.031481
Exposed	0.8, 6.6	-0.214491	0.676345	-0.944853	1.797528	-3.466392	3.153009	1.294033	-1.854967
Exposed	0.1, 0.4	0.409300	-2.012155	2.914548	0.082785	-3.720081	3.149134	0.979763	-1.349478
Partially sheltered	0.01, 0.1	-0.165456	0.192382	0.312596	-0.147988	-0.832178	1.204086	0.968676	-0.898683
Partially sheltered	0.8, 6.6	0.954423	-2.881124	1.105712	3.811321	-4.095948	0.928698	2.620931	-2.017396
Partially sheltered	0.1, 0.4	0.299556	-1.026644	0.263271	2.243460	-2.432358	0.369177	2.133429	-1.352123
Sheltered	0.01, 0.1	-25.023587	17.512051	29.169293	-17.342279	-9.368972	3.515141	2.456428	-0.505570
Sheltered	0.8, 6.6	16.848436	-26.898163	1.761651	13.096786	-4.680737	-0.167992	2.646008	-1.846077
Sheltered	0.1, 0.4	-11.611438	5.978572	17.545307	-6.926464	-8.811607	2.482293	3.170563	-1.250451

There is a model for each of the three frequency bands and each of the three land cover categories. The columns  $c_1-c_8$  denote each of the coefficients for the seventh-degree polynomial.



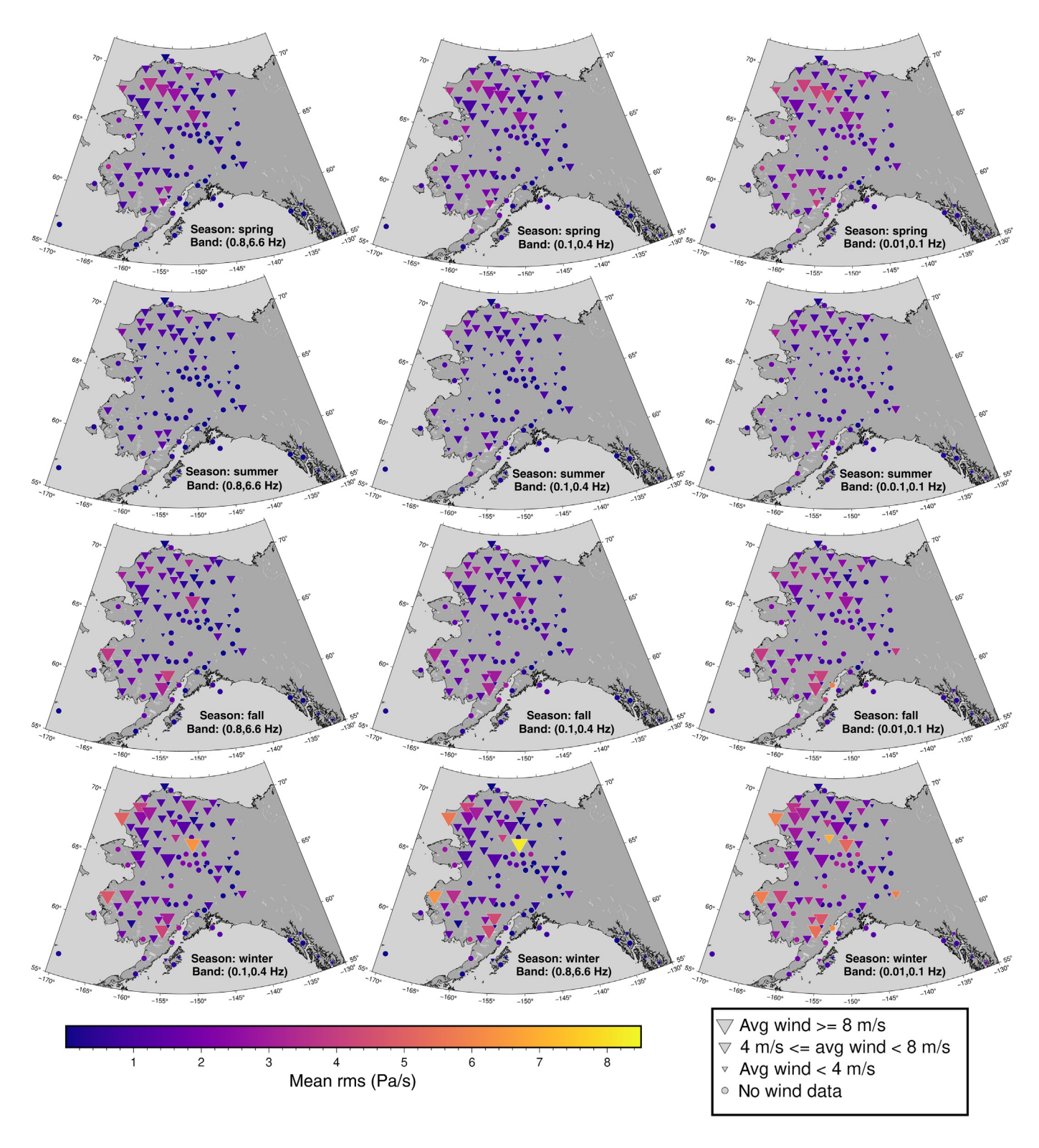
**Figure 5.** Infrasound ambient noise model for the Alaska region. Light blue curves are the 95th-percentile power spectral densities (PSDs) from all the contributing stations, whereas 5th-percentile curves are shown in gray. The new low- and high-noise models are shown in solid dark blue, whereas the median is shown in dashed dark blue. The International Data Center global ambient noise model from Brown *et al.* (2012) is shown in dashed orange for reference. The color version of this figure is available only in the electronic edition.

#### Insights from rms time series

Mapping the 2020 average rms for each station provides a general overview of the spatial distribution of rms amplitudes. Maps of rms organized by season and passband are shown in Figure 6. Stations are colored by average rms, whereas symbol size is scaled by the mean wind speed, grouped into three bins, for stations with available weather data. Seasons are

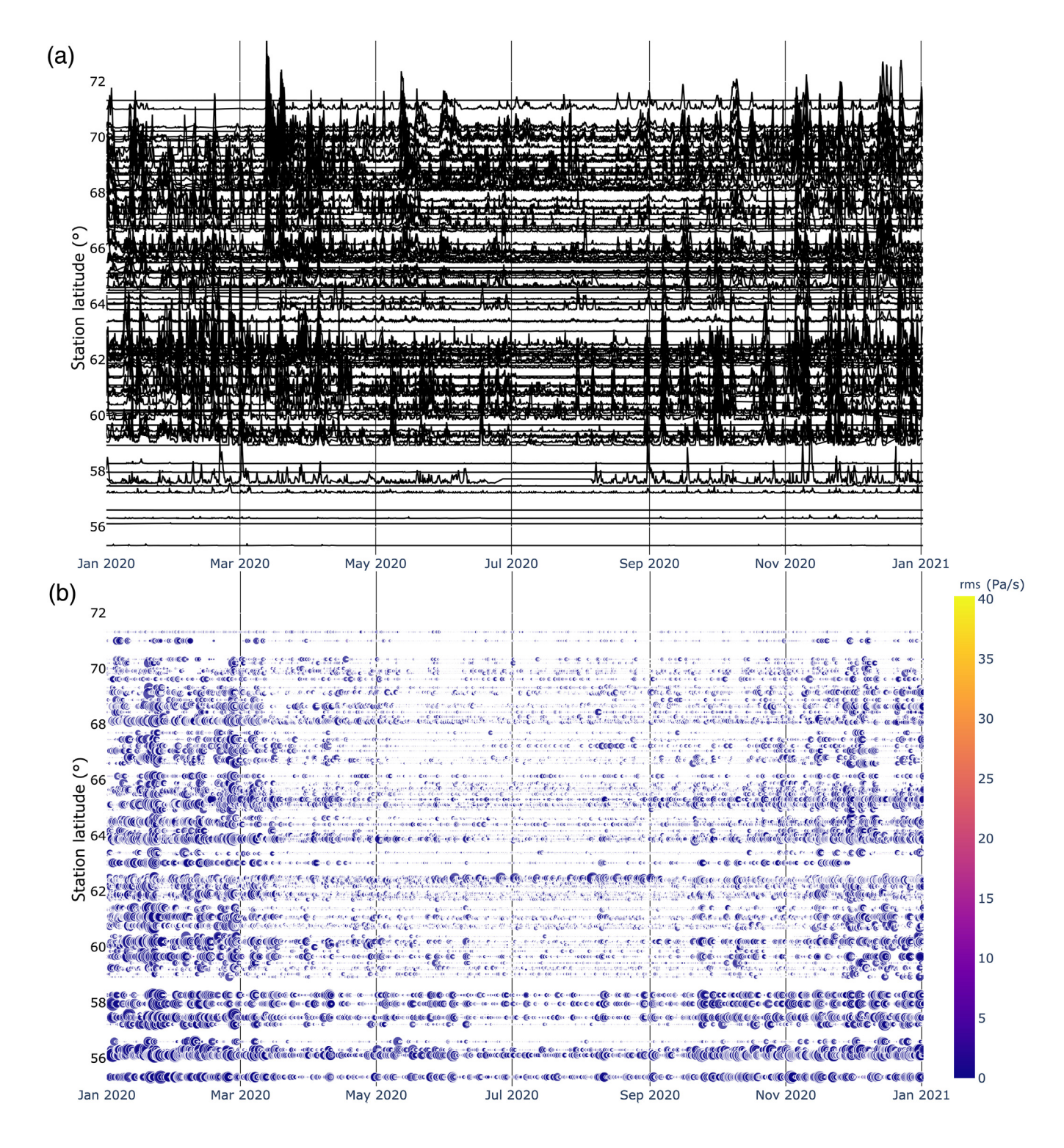
defined as November, December, and January for winter; February, March, and April for spring; May, June, and July, for summer; and August, September, and October for fall. In the following, we focus our in-text discussion on the the high-frequency passband, but all the three passbands share similar temporal and spatial patterns. In general, the summer experiences the lowest average wind speeds and rms amplitudes, whereas winter exhibits the highest. The fall and spring seasons not only generally exhibit an intermediate level of average wind speeds and noise but also show some interesting differences between the two seasons. The spring season appears to be characterized by higher wind speed and higher rms amplitudes in northern Alaska, whereas the fall season sees higher values in the southwest of the state. These patterns persist across all the three passbands, and this is probably a result of the pink spectral nature of windinduced noise. The spatial pattern in the maps of the winter season encouraged us to consider a correlation between rms amplitude and distance to the nearest coastline, but we were not able to observe any clear dependence between these two parameters.

We use our rms time series with a four-hour sampling rate at each AK station to investigate seasonal and geographical effects at a higher temporal resolution. These time series are shown in Figure 7a, with amplitudes normalized across the network to highlight relative noise differences between stations and with each trace organized by station latitude. This view allows us to examine a year of rms amplitudes across the entire network, and several notable features stand out. The five stations located in southeastern Alaska are consistently quiet, relative to the rest of the network for the entire year (most traces below 58.3°). This may be a result of the dense tree cover in that region of the state. Another



ubiquitous feature in the plots is large-amplitude spikes that are fairly discrete in time but widely observed across the network (e.g., there is an array-wide spike in mid-November 2020). We interpret these as wind-induced amplitude anomalies associated with large storms moving across the region. These spikes are more common in cold weather (October–April) relative to summer months (May–September), when there is a decreased storm activity in the northern

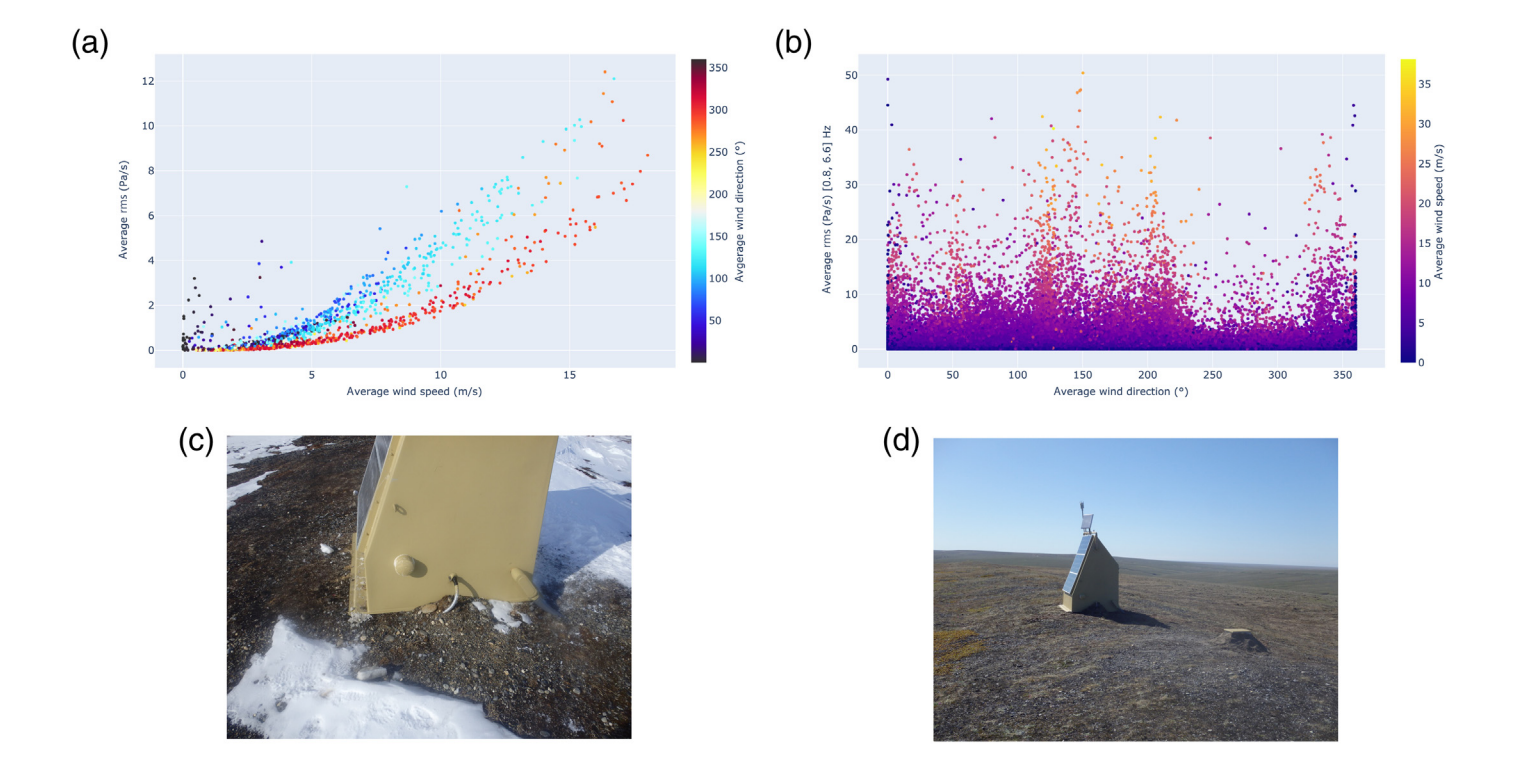
**Figure 6.** Maps of seasonal average infrasound rms for the entire 2020 study period. The four rows are organized by season, whereas the three columns correspond to the three passbands: [0.01, 0.1], [0.1, 0.4], and [0.8, 6.6] Hz. The three symbols sizes correspond to average wind speed bins defined by cutoffs of 8 and 4 m/s. The color version of this figure is available only in the electronic edition.



hemisphere. Similar figures for the lower frequency passbands are included in Figure A4.

There is also a strong seasonal signal affecting the presence of the microbarom in the spectra. This is to be expected, as seasonal variations in microbarom source zones have been observed in previous studies (e.g., Landès *et al.*, 2012; Landès *et al.*, 2014). At most of the sites, the amount of spectral curvature in the microbarom band of 0.1–0.4 Hz (see Fig. 7b) is larger in the winter months. There are many more linear

**Figure 7.** (a) RMS amplitude time series in the [0.8, 6.6] Hz passband for all the 104 stations for 2020. Traces are organized vertically by the latitude of each station. Similar figures for the [0.01, 0.1], and [0.1, 0.4] Hz passbands are provided in the Appendix, although general trends are similar. Amplitudes have been normalized across the network. (b) Time series of circles scaled by the residual of fitting a line to the hourly PSD in the [0.1, 0.4] Hz passband for 2020. Larger dots represent time periods when the microbarom was more likely present. Dots are colored by rms in the [0.1, 0.4] Hz passband. The color version of this figure is available only in the electronic edition.



spectra in the summer, indicating that the microbarom is weaker despite the reduced rms amplitude. Stations in the southeast that have consistently lower noise levels exhibit many time periods in which the microbarom is likely present, even throughout the summer months. One station, NEA2, was removed from Figure 7b due to the fact that its microbarom band is contaminated by a spectral peak imposed by a nearby communications tower during periods of high wind (Smith and Tape, 2019).

We also investigate the effect of wind direction on noise. Although it is more difficult to draw general network-wide conclusions about this parameter, we did observe a clear dependence of rms amplitudes on wind direction at several stations, at which wind azimuths from the east imposed a higher rms than azimuths from the west for comparable wind speeds (see Fig. 8a for an example). To determine if this is a general feature of the network, we plot rms as a function of average wind speed for the [0.8, 6.6] Hz passband (Fig. 8b). This plot reveals generally lower rms amplitudes for winds from westerly directions. We believe this may be a result of the diffuser port being mounted on the east side of the hut for all the stations, an example of which can be seen in Fig. 8c on an exposed station (Fig. 8d). This configuration puts the port on the lee side of the hut when the wind is from the west, whereas easterly winds interact with the port directly.

These network-wide observations illustrate that the rms amplitudes are highly dependent on wind speed, which is not surprising, given the absence of WNRS and the fact that many stations are located in exposed environments (e.g., Fig. 8d). The generally lower rms for sites in dense foliage or

**Figure 8.** (a) Average hourly rms as a function of hourly average wind speed at station C26K—a station with a clear relationship between wind direction and rms. Dots are colored by hourly average wind direction. (b) Scatter plot showing relationship between rms in the [0.8, 6.6] Hz passband and wind direction. Dots are colored by hourly average wind speed. (c) Image of station C26K showing configuration of the diffuser port. (d) Local conditions at C26K showing station exposure. The color version of this figure is available only in the electronic edition.

forest also indicates that noise performance is dependent on land cover type.

## Results of modeling noise as a function of wind speed and land cover

Because rms is clearly dependent on site land cover type and wind speed, models incorporating these parameters will be a reliable method for predicting infrasound station noise. We test the efficacy of our wind-noise relationships using wind speed and land cover type to estimate the rms amplitudes at several stations. We apply the models to a five-month period from 2021, to avoid testing on data that was used to derive the models. RMS is estimated at a sheltered site, M23K in south-central Alaska, a partially sheltered site, J25K in interior Alaska, and an exposed site, N19K, in the western Alaska range (see Fig. 1). The observed rms, estimated rms, and smoothed (low-pass Butterworth filter with a 12 hr corner) hourly average wind speeds for a five-month period of 2021 are shown in Figure 9. There is a clear correlation between rms amplitude

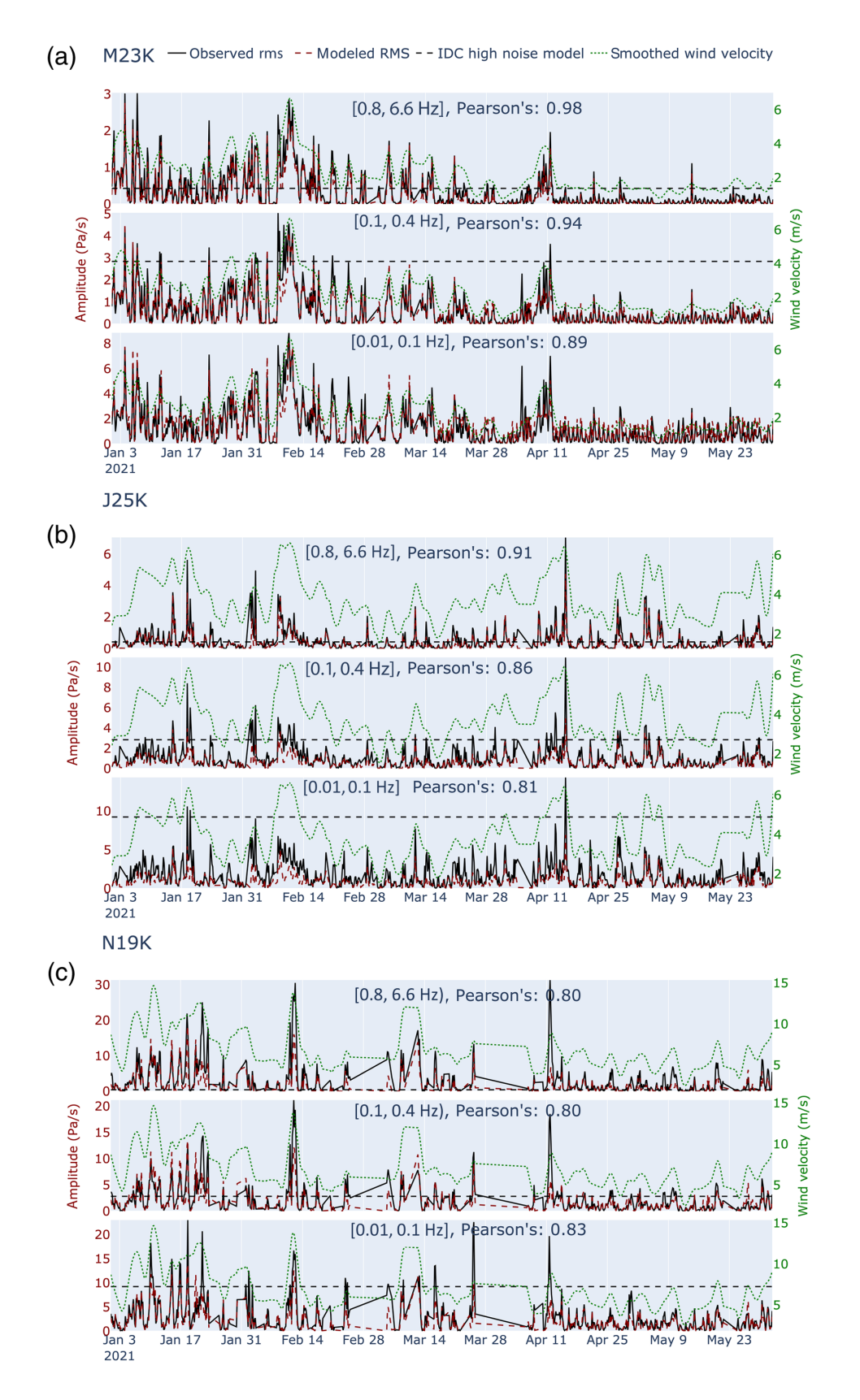


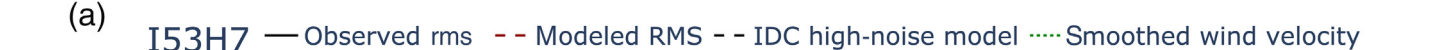
**Figure 9.** Comparison of observed (solid black lines) and modeled (dashed red lines) rms values at three AK infrasound stations. (a) M23K, a sheltered site. (b) J25K, a partially sheltered site. (c) N19K, an exposed site. Green line shows filtered hourly wind speed. Each station subpanel shows results for a different passband. The rms amplitude from the IDC noise model for each band is indicated by a dashed horizontal black line (if on scale). The color version of this figure is available only in the electronic edition.

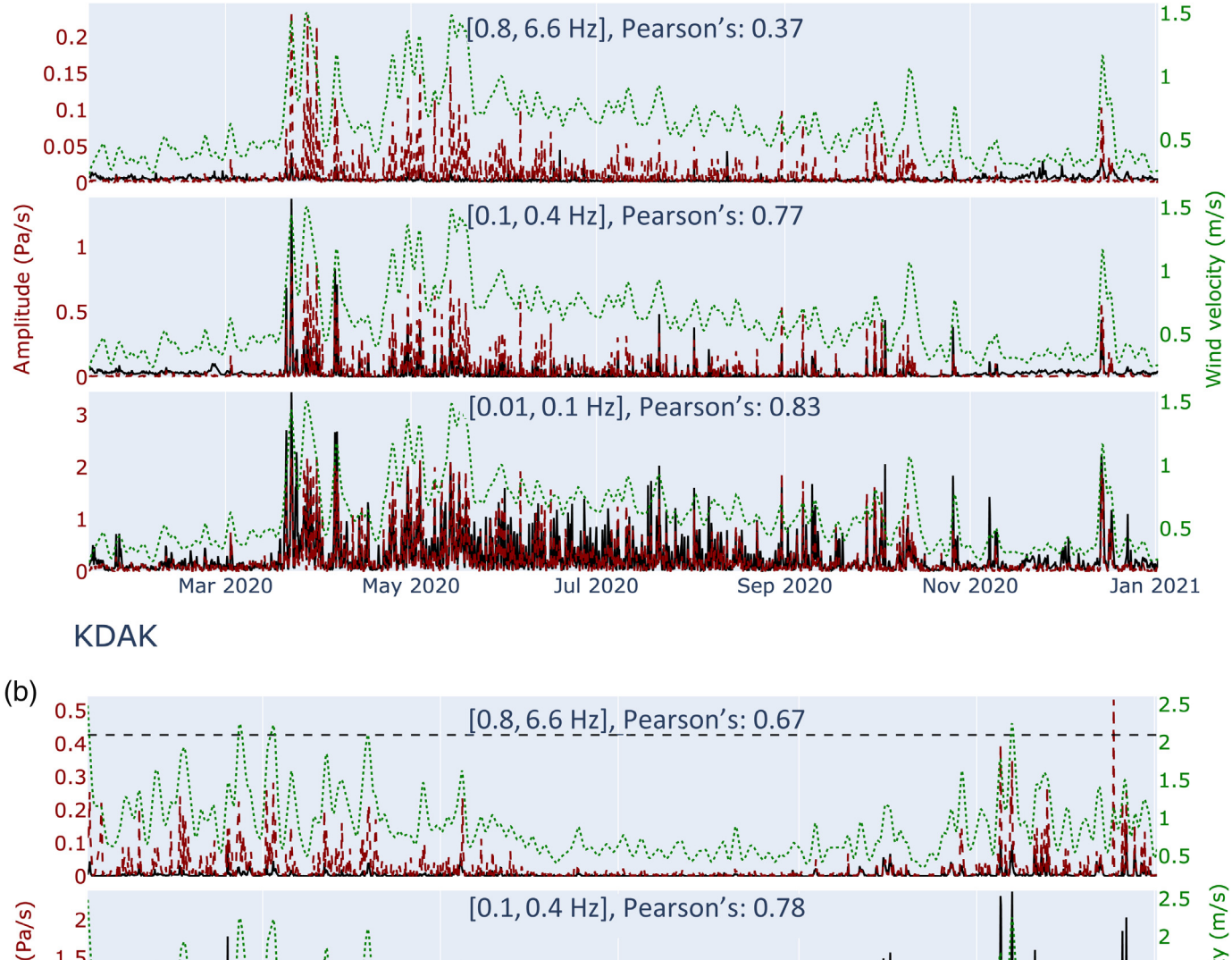
and wind speed, although the accuracy varies between land cover category. Each panel shows the results for a particular passband, and waveform similarities are quantified by the Pearson's correlation coefficient, which is the normalized covariance and indicates the linear correlation between the two quantities.

The results for both M23K and J25K show that the models accurately estimate the rms amplitudes as a function of wind speed in all the three frequency bands. The models are particularly effective in the [0.8, 6.6] Hz band, with Pearson's correlation values near 1.0 for the sheltered and partially sheltered sites. Models are somewhat less effective in the low-frequency passband, and this may indicate a significant contribution of other signals to amplitudes at these periods. The least-robust model performance is for the exposed site, N19K, but we still achieve Pearson's values of around 0.8. Wind data for this and many of the exposed sites are poor, and many data were discarded as a result of our QC process. During periods with high-quality data, in early January, for example, the model results agree closely with the observations (see Fig. 9).

#### **Discussion**

The ambient AK noise model reflects the range of noise levels imposed by Alaska's diverse geography. The noise-wind models illustrate that wind is the dominant source of background noise for the network, as expected, given the station's lack of WNRS and the fact that many of them are situated in





high-wind areas. The models also demonstrate that site land cover type is an important control on rms amplitudes and, consequently, on station performance. Therefore, noise—wind models that incorporate land cover type have potential for evaluating station performance. By monitoring model fits, operators can be alerted to potential problems when rms deviates substantially from model-predicted values. The models also have utilty

**Figure 10.** Comparison of observed and modeled rms values at two non-AK stations. (a) I53H7, a sheltered site that is part of the IMS. (b) KDAK, a sheltered site that is part of the GSN. Green line shows filtered hourly wind speed. Each station subpanel shows results for a different passband. The rms amplitude from the IDC noise model for each band is indicated by a dashed horizontal black line (if on scale). The color version of this figure is available only in the electronic edition.

for future site placement, as noise levels may be estimated at potential sites if land cover and wind speed data are available.

To investigate if the rms-wind modeling relationship has applicability beyond the Alaska region, we modeled noise at an IMS site, I53H7 (Fairbanks, Alaska), and at a Global Seismographic Network (GSN) station, KDAK (Kodiak, Alaska) (see Fig. 1) (Scripps Institution of Oceanography, 1986). Both the stations are located in sheltered land cover types and are equipped with WNRS. The comparison of modeled to observed rms amplitudes is shown in Figure 10. For I53H7, the model performs poorly at high frequencies but improves substantially in the lower frequency bands. This is to be expected, due to the fact that IMS WNRS systems are effective primarily above approximately 0.1 Hz, below which the length of the filter is comparable to the noise coherence length (Raspet et al., 2019). The relatively good performance of the models for the low-frequency bands indicates that they are applicable beyond the AK regional network. The model results for KDAK are more difficult to interpret. The high-frequency model is the poorest performer, as expected, but does not differ as drastically from other bands as did the results for I53H7. This may be a result of differences in WNRS equipment employed by the GSN and IMS. Performance in the lowest frequency band for this station is poor, with a Pearson's correlation of 0.71, which is unexpected and in contrast to the 0.83 value for the low-frequency band at I53H7. Much of the misfit appears to be a result of noise spikes that do not appear correlated with increased wind speeds. This is, particularly, visible in the time period from late September into October. Here, we observe large-amplitude anomalies in rms in the low-frequency bands, but with subdued wind speeds, whereas there are relatively low rms amplitudes in the high-frequency band. We conclude that poor model fits in this frequency band are a result of the presence of noise from sources other than wind.

While wind direction does not exhibit as dramatic control on rms amplitudes as wind speed, we did observe a correlation between higher amplitudes for a given wind speed for westerly winds at exposed sites. We conclude that this is a result of the diffuser being located on the lee side of the hut during westerly winds. Stagnation pressure, caused by interaction of wind-related turbulence on the hut itself (Raspet et al., 2019), is likely causing the increased noise when the diffuser is exposed directly to the wind. We observe these results strongly suggest that infrasound station performance may be affected by the location of the port on the hut, and encourage future installations to port the sensor to the atmosphere away from the hut and other obstacles, or install multiple ports. We also observe that the diffuser is elevated above the surface and suggest future installations be ported closer to the ground where the wind noise will likely be lower (Raspet et al., 2019).

#### **Conclusions**

We analyzed all available 2020 infrasound data from network AK to characterize the ambient infrasonic environment of the Alaska region, east of −170° longitude. The network encompasses a diverse range of environments, many of which are suboptimal for infrasound data quality. We leveraged this diversity along with the absence of WNRS at these stations to build an ambient infrasound model for the Alaska region and to quantify the effects of site conditions on infrasound noise. Our low-noise model has a shape and amplitude similar to the IDC model from Brown et al. (2012), but our high-noise model deviates significantly, particularly at frequencies above 0.1 Hz, in which the WNRS of the IMS stations are effective. Infrasound models derived from stations without WNRS are rare, although recent work by Marty et al. (2021) presented models from data with the response of the WNRS removed during processing. Our new models and those of Marty et al. (2021) are similar, even at higher frequencies. Although models that contain unfiltered wind noise may be inappropriate for QC of IMS stations, they do provide a more general estimate of ambient noise at low frequencies. This makes our new model highly useful for evaluating noise performance of the growing number of infrasound stations that may not have as robust spatial filtering as IMS stations.

Time series of rms noise for all the stations reveal a strong seasonal signal, with the network exhibiting generally lower amplitudes in the summer months than the winter months. High-noise periods tend to be dominated by high-amplitude, temporally discrete spikes that we interpret as being imposed by high-wind speeds associated with large storms. We also observe a stronger microbarom across the network during the winter months, which is consistent with seasonal pattern for northern latitude stations observed by Landès *et al.* (2012) and Landès *et al.* (2014). We observe that some stations are consistently noisy relative to the rest of the network (e.g., N19K), whereas others, such as those in southeast Alaska, are consistently quieter, and this is likely due to the effect of local land cover types attenuating wind.

Because we observed that rms noise amplitudes are dependent on land cover type and wind speed, we developed models for three broad land cover classifications that estimate rms amplitude as a function of wind speed. We found that these models accurately predict station noise levels for the three considered frequency bands. These models are also effective for stations equipped with IMS-style WNRS at periods longer than about 10 s. Models that incorporate wind speed and site land cover class are effective tools for predicting future site noise performance and for infrasound station site selection.

Although not incorporated into our models, we also observe that wind direction can influence station noise levels. This seems to be a result of the configuration of AK stations in which the infrasound diffuser is mounted consistently on the east side of the hut, so that the structure attenuates wind from westerly directions, while fully exposing the diffuser to easterly gusts. We recommend future deployments position the infrasound port as far from the hut or other structures as is practicable. Another option would be to locate the diffuser on the lee side of the hut, if prevailing wind direction is known.

We have constructed an ambient infrasound model for the Alaska region that is broadly applicable for infrasound station data QC. From this model, we developed robust relationships between infrasound rms amplitudes, wind speed, and site land cover type. These constitute effective tools and strategies that may be leveraged for infrasound QC, noise prediction, and station location selection.

#### **Data and Resources**

All Infrasound and wind data used in this study were produced by the networks of the USArray Transportable Array project (DOI: 10.7914/ SN/TA), the Alaska Earthquake Center (DOI: 10.7914/SN/AK), the Global Seismographic Network (DOI: 10.7914/SN/II), and the International Miscellaneous Stations, and these data are available from the Incorporated Research Institutions for Seismology (IRIS) Data Management Center (DMC) (http://ds.iris.edu/ds/nodes/dmc/; last accessed December 2021). Land cover classification data are from the National Land Cover Database (DOI: 10.5066/P96HHBIE) and were downloaded from the Multi-Resolution Land Characteristics Consortium website (https://www.mrlc.gov/data/nlcd-2016-landcover-alaska; last accessed July 2021). This project relied heavily on free and open-source software packages, including ObsPy (DOI: 10.5281/zenodo.3706479) and PyGMT (DOI: 10.5281/zenodo. 5607255) (Wessel et al., 2019). Supplemental material for this article consists of new ambient infrasound low- and high-noise models in comma-delimited text format.

### **Declaration of Competing Interests**

The authors acknowledge that there are no conflicts of interest recorded.

### **Acknowledgments**

The authors acknowledge the Alaska Native nations upon whose land our study area resides and observe the stewardship of the traditional inhabitants of the region. This research was supported by the Defense Threat Reduction Agency Nuclear Arms Control Technology program under Contract HQ003421F0112 and HDTRA121C0030 (distribution statement: cleared for release), National Science Foundation Award number 2024208, and the National Mesonet program at the University of Alaska Fairbanks (UAF). The authors thank Adam Ringler at the Albuquerque Seismological Laboratory and an anonymous reviewer for helpful comments that improved the final article. This article also benefited from conversations with members of the Wilson Alaska Technical Center at UAF and with Amy Macpherson at the Alaska Department of Natural Resources.

#### References

Alaska Earthquake Center, University of Alaska Fairbanks (1987). Alaska regional network, doi: 10.7914/SN/AK.

- Alcoverro, B., and A. Le Pichon (2005). Design and optimization of a noise reduction system for infrasonic measurements using elements with low acoustic impedance, *J. Acoust. Soc. Am.* 117, no. 4, 1717–1727, doi: 10.1121/1.1804966.
- Beyreuther, M., R. Barsch, L. Krischer, T. Megies, Y. Behr, and J. Wassermann (2010). ObsPy: A Python toolbox for seismology, *Seismol. Res. Lett.* **81**, no. 3, 530–533, doi: 10.1785/gssrl.81.3.530.
- Bird, E. J., D. C. Bowman, D. R. Seastrand, M. A. Wright, J. M. Lees, and F. K. Dannemann Dugick (2021). Monitoring changes in human activity during the COVID-19 shutdown in Las Vegas using infrasound microbarometers, J. Acoust. Soc. Am. 149, no. 3, 1796–1802, doi: 10.1121/10.0003777.
- Bowman, J. R., G. E. Baker, and M. Bahavar (2005). Ambient infrasound noise, *Geophys. Res. Lett.* **32**, no. 9, 1–5, doi: 10.1029/2005GL022486.
- Brown, D., L. Ceranna, M. Prior, P. Mialle, and R. J. L. Bras (2012). The IDC seismic, hydroacoustic and infrasound global low and high noise models, *Pure Appl. Geophys.* **171**, nos. 3/5, 361–375, doi: 10.1007/s00024-012-0573-6.
- Busby, R. W., and K. Aderhold (2020). The Alaska Transportable Array: As built, *Seismol. Res. Lett.* **91,** no. 6, 3017–3027, doi: 10.1785/0220200154.
- Casey, R., M. E. Templeton, G. Sharer, L. Keyson, B. R. Weertman, and T. Ahern (2018). Assuring the quality of IRIS data with MUSTANG, Seismol. Res. Lett. 89, no. 2A, 630–639, doi: 10.1785/0220170191.
- Christie, D. R., and P. Campus (2009). The IMS infrasound network: Design and establishment of infrasound stations, in *Infrasound Monitoring for Atmospheric Studies*, A. Le Pichon, E. Blanc, and A. Hauchecorne (Editors), Springer Netherlands, Dordrecht, 29–75.
- Christie, D. R., J. A. Vivas Veloso, P. Campus, M. Bell, T. Hoffmann, A. Langlois, P. Martysevich, E. Demirovic, and J. Carvalho (2001). Detection of atmospheric nuclear explosions: The infrasound component of the International Monitoring System, *Kerntechnik* **66**, no. 3, 96–101.
- de Groot-Hedlin, C. D., M. A. H. Hedlin, and D. P. Drob (2010). Atmospheric variability and infrasound monitoring, in Infrasound Monitoring for Atmospheric Studies, A. Le Pichon, E. Blanc, and A. Hauchecorne (Editors), Springer Netherlands, Dordrecht, 475–507.
- Dewitz, J. (2019). National Land Cover Dataset (NLCD) 2016 products, doi: 10.5066/P96HHBIE.
- Donn, W. L., and E. S. Posmentier (1967). Infrasonic waves from the marine storm of April 7, 1966, *J. Geophys. Res.* **72**, no. 8, 2053–2061, doi: 10.1029/JZ072i008p02053.
- Fee, D., and R. S. Matoza (2013). An overview of volcano infrasound: From Hawaiian to Plinian, local to global, *J. Volcanol. Geotherm. Res.* **249**, 123–139, doi: 10.1016/j.jvolgeores.2012.09.002.
- Green, D. N., and D. Bowers (2010). Estimating the detection capability of the International Monitoring System infrasound network, *J. Geophys. Res.* **115**, no. D18, doi: 10.1029/2010JD014017.
- Gubbins, D. (2004). Time Series Analysis and Inverse Theory for Geophysicists, Cambridge University Press, Cambridge, England.
- Guenaga, D. L., O. E. Marcillo, A. A. Velasco, C. Chai, and M. Maceira (2021). The silencing of U.S. campuses following the COVID-19 response: Evaluating root mean square seismic amplitudes using power spectral density data, *Seismol. Res. Lett.* 66, no. 3, doi: 10.1785/0220200391.

- IRIS Transportable Array (2003). USArray Transportable Array [dataset], doi: 10.7914/SN/TA.
- Krischer, L., T. Megies, R. Barsch, M. Beyreuther, T. Lecocq, C. Caudron, and J. Wassermann (2015). ObsPy: A bridge for seismology into the scientific Python ecosystem, *Comput. Sci. Discov.* 8, no. 1, 014003, doi: 10.1088/1749-4699/8/1/014003.
- Landès, M., L. Ceranna, A. Le Pichon, and R. S. Matoza (2012). Localization of microbarom sources using the IMS infrasound network, J. Geophys. Res. 117, no. D6, doi: 10.1029/2011JD016684.
- Landès, M., A. Le Pichon, N. M. Shapiro, G. Hillers, and M. Campillo (2014). Explaining global patterns of microbarom observations with wave action models, *Geophys. J. Int.* 199, no. 3, 1328– 1337, doi: 10.1093/gji/ggu324.
- Le Pichon, A., L. Ceranna, and J. Vergoz (2012). Incorporating numerical modeling into estimates of the detection capability of the IMS infrasound network, *J. Geophys. Res.* **117**, no. D5, doi: 10.1029/2011JD016670.
- Le Pichon, A., J. Vergoz, E. Blanc, J. Guilbert, L. Ceranna, L. Evers, and N. Brachet (2009). Assessing the performance of the International Monitoring System's infrasound network: Geographical coverage and temporal variabilities, *J. Geophys. Res.* 114, no. D8, doi: 10.1029/2008JD010907.
- Lecocq, T., S. P. Hicks, K. Van Noten, K. van Wijk, P. Koelemeijer, R. S. M. De Plaen, F. Massin, G. Hillers, R. E. Anthony, M.-T. Apoloner, *et al.* (2020). Global quieting of high-frequency seismic noise due to COVID-19 pandemic lockdown measures, *Science* 369, no. 6509, 1338–1343, doi: 10.1126/science.abd2438.
- Marty, J., B. Doury, and A. Kramer (2021). Low and high broadband spectral models of atmospheric pressure fluctuation, *J. Atmos. Ocean. Technol.* **38,** no. 10, 1813–1822, doi: 10.1175/JTECH-D-21-0006.1.
- McNamara, D. E., and R. P. Buland (2004). Ambient noise levels in the continental united states, *Bull. Seismol. Soc. Am.* **94**, no. 4, 1517–1527, doi: 10.1785/012003001.
- Melter, A., R. Rudnick, P. Zeitler, A. Levander, G. Humphreys, K. Karlstrom, G. Ekstrom, R. Carlson, T. Dixon, M. Gurnis, *et al.* (1999). USArray initiative, *GSA Today* **9**, no. 11, 40.
- Merchant, B. J. (2015). Hyperion 5113/GP Infrasound Sensor Evaluation, Technical Report SAND-2015-7075, Sandia National Lab. (SNL-NM), Albuquerque, NM (United States), doi: 10.2172/ 1213302.
- Raspet, R., J.-P. Abbott, J. Webster, J. Yu, C. Talmadge, K. Alberts, II, S. Collier, and J. Noble (2019). New systems for wind noise reduction for infrasonic measurements: Challenges in middle atmosphere

- dynamics and societal benefits, in *Infrasound Monitoring for Atmospheric Studies*, 91–124, doi: 10.1007/978-3-319-75140-5\_3.
- Scripps Institution of Oceanography (1986). Global seismograph network—IRIS/IDA, doi: 10.7914/SN/II.
- Smith, K., and C. Tape (2019). Seismic noise in central Alaska and influences from rivers, wind, and sedimentary basins, *J. Geophys. Res.* **124**, no. 11, 11,678–11,704, doi: 10.1029/2019JB017695.
- Virtanen, P., R. Gommers, T. E. Oliphant, M. Haberland, T. Reddy, D. Cournapeau, E. Burovski, P. Peterson, W. Weckesser, J. Bright, et al. (2020). SciPy 1.0: Fundamental algorithms for scientific computing in Python, Nat. Methods 17, 261–272, doi: 10.1038/s41592-019-0686-2.
- Walker, K. T., and M. A. Hedlin (2010). A review of wind-noise reduction methodologies, in *Infrasound Monitoring for Atmospheric Studies*, A. Le Pichon, E. Blanc, and A. Hauchecorne (Editors), Springer Netherlands, Dordrecht, 141–182.
- Wessel, P., J. F. Luis, L. Uieda, R. Scharroo, F. Wobbe, W. H. F. Smith, and D. Tian (2019). The Generic Mapping Tools version 6, Geochem. Geophys. Geosys. 20, no. 11, 5556–5564, doi: 10.1029/2019GC008515.

### **Appendix**

This section provides additional figures not included in the main text. There is a detailed image of a typical



**Figure A1.** Deatiled image of the diffuser port at station I23K in Minto Alaska. This configuration is typical of Alaska Transportable Array stations. The color version of this figure is available only in the electronic edition.

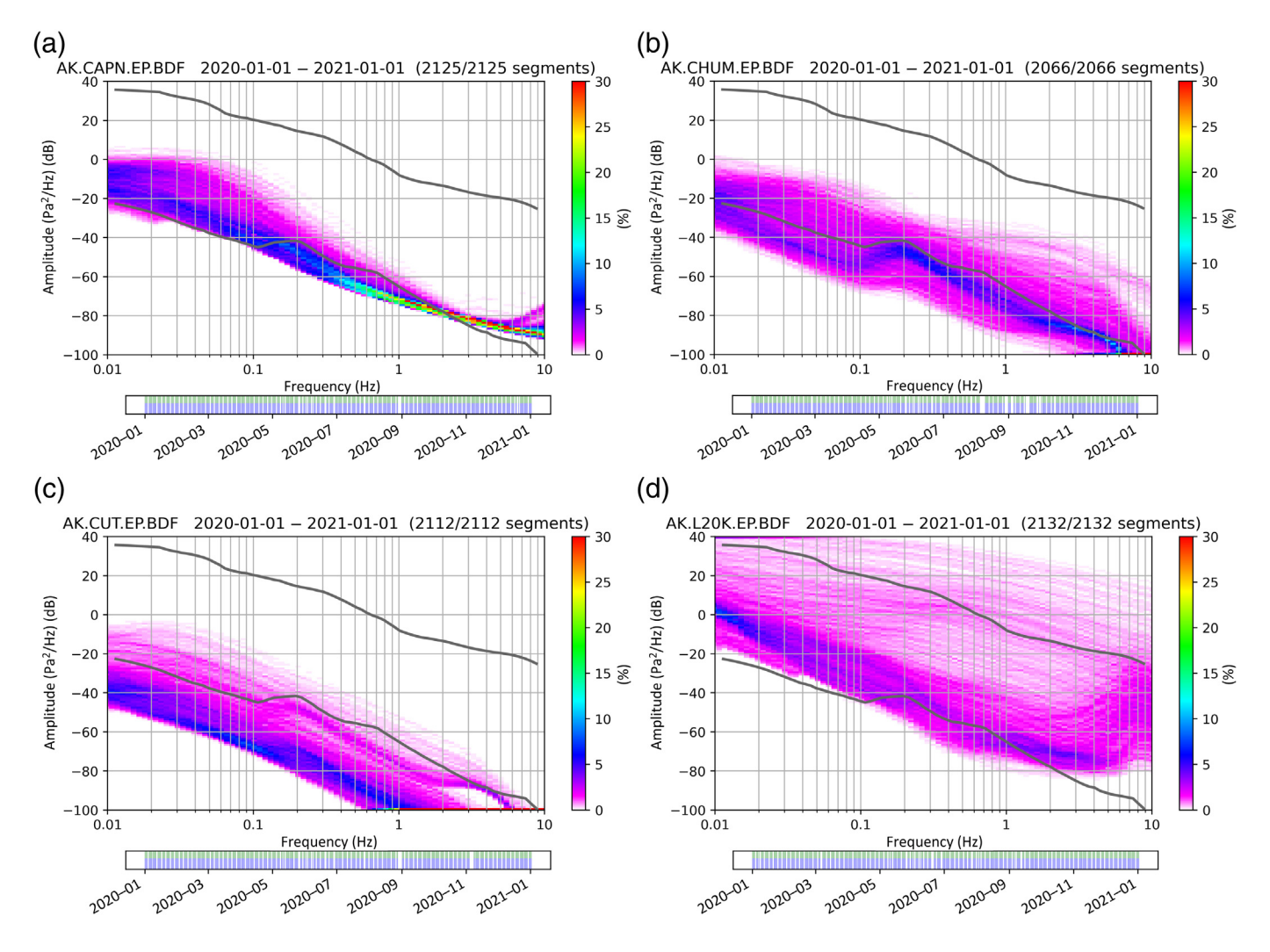


**Figure A2.** Power spectral density probability density function (PDF) plots of the four stations identified to have response issues. All four stations, (a) CAPN, (b) CHUM, (c) CUT, and (d) L20K have unrealistically low amplitudes. The International Data Center

high- and low-noise models are plotted as black lines. Bar in bottom of each plot shows the time ranges with data that contributed to the PDF. The color version of this figure is available only in the electronic edition.

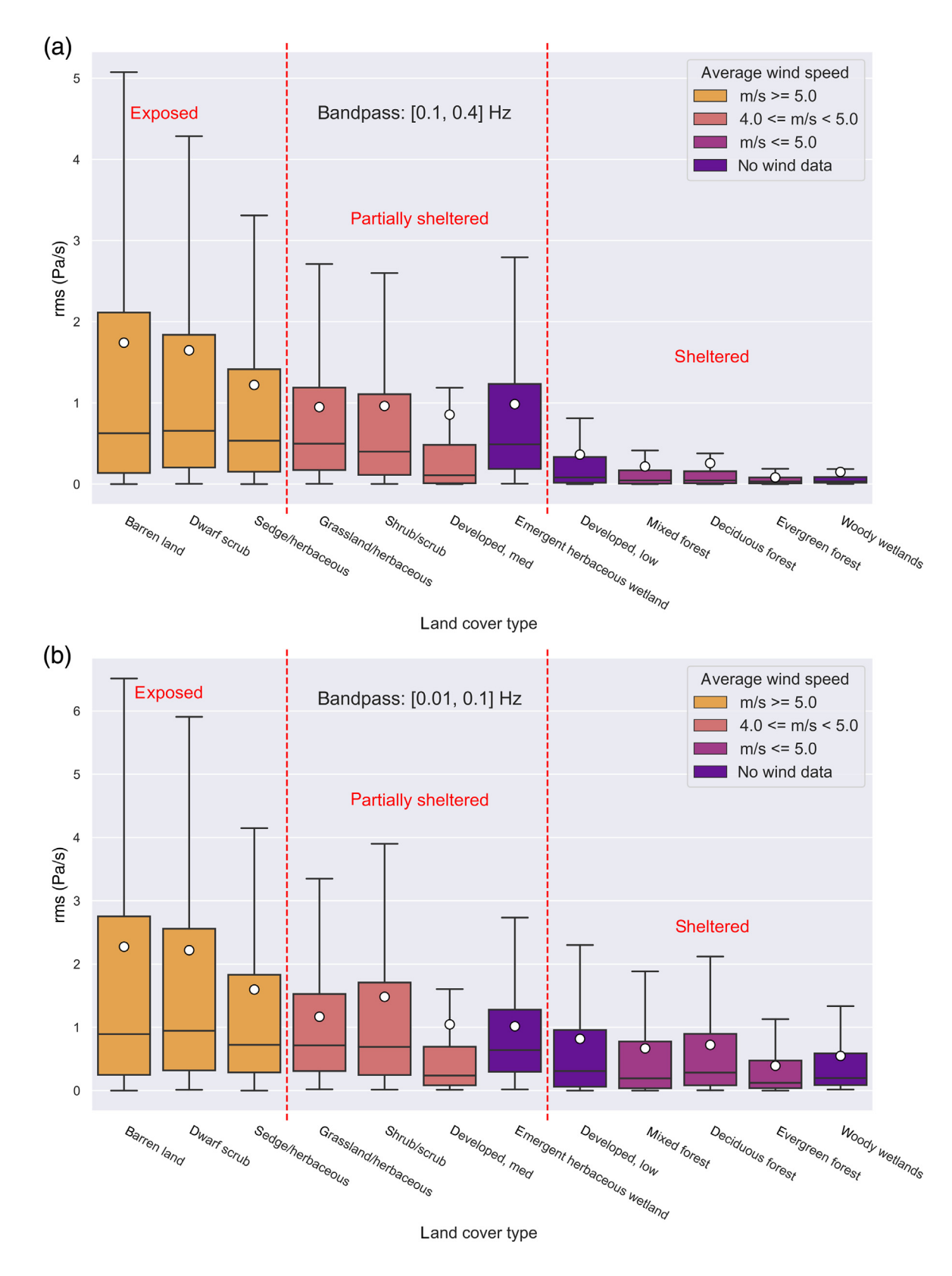


**Figure A3.** Root-mean-squared (rms) infrasound amplitude for 2020 binned by station land cover for the (a) [0.1, 0.4] and (b) [0.01, 0.1] Hz passbands. The upper and lower edges of the boxes denote the third and first quartiles, respectively. The horizontal line in each box denotes the medians, whereas the

means are shown by white circles. The bars extend to 1.5 times the interquartile range. For clarity, outliers are not plotted. Boxes are colored by mean wind speed categories from 2020 data. The color version of this figure is available only in the electronic edition.

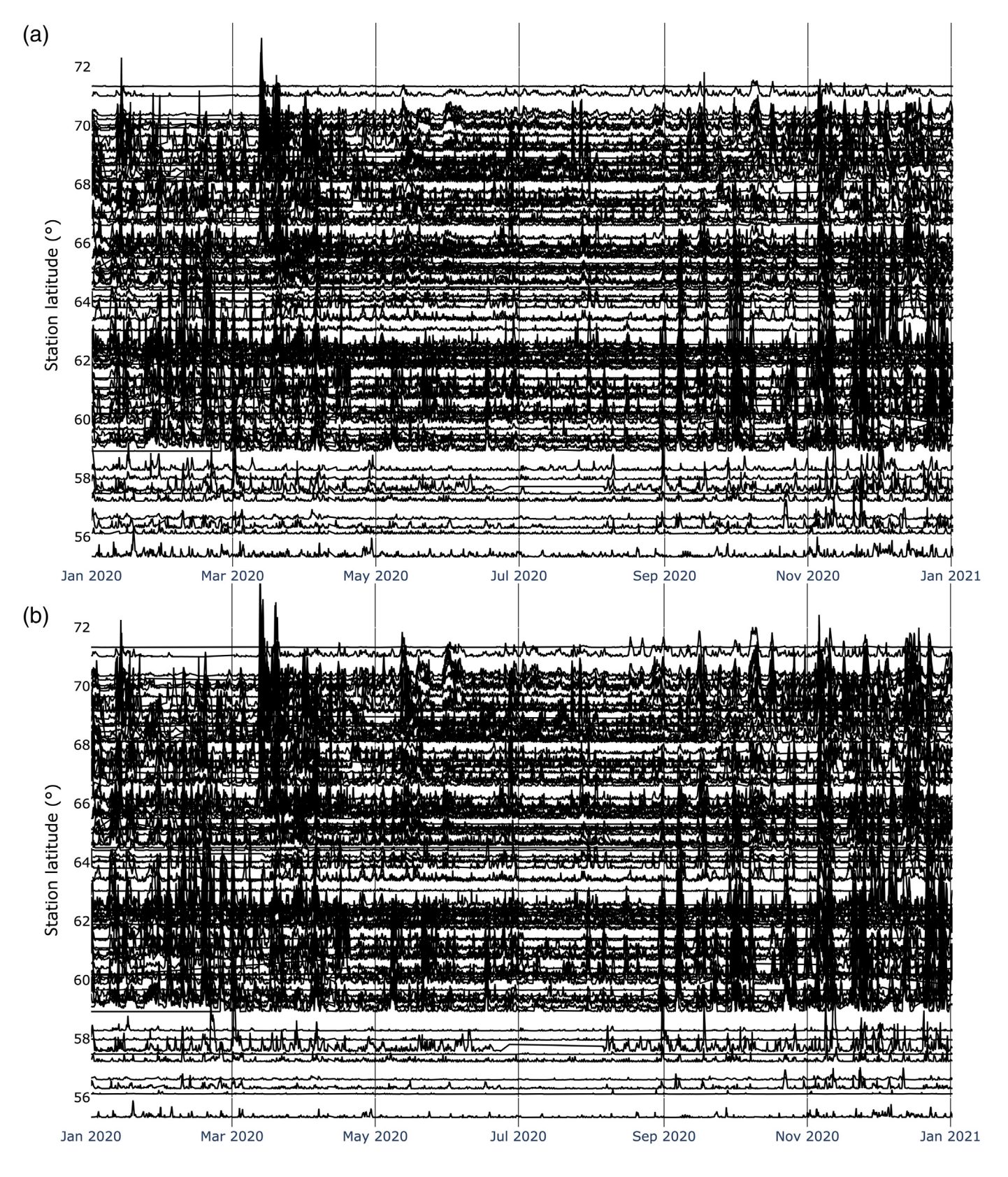


**Figure A4.** Globally normalized rms infrasound amplitude time series in the (a) [0.01, 0.1] and (b) [0.1, 0.4] Hz passbands for all 104 AK infrasound stations in 2020. Traces are organized

vertically by the latitude of each station. The color version of this figure is available only in the electronic edition.

Transportable Array infrasound diffuser port. There are power spectral density probability density function plots of the four poorly performing AK infrasound stations that were removed from further analysis. There are also figures of root-mean-squared (rms) time series and rms binned by land

cover type for all the stations for passbands not included in the main text.

Manuscript received 21 December 2021 Published online 19 April 2022